The Near-Ultraviolet Spectra of FU Orionis Accretion Disks

ADOLFO S. CARVALHO, LYNNE A. HILLENBRAND, GREGORY J. HERCZEG, 2,3 AND KEVIN FRANCE

¹Department of Astronomy; California Institute of Technology; Pasadena, CA 91125, USA

²Kavli Institute for Astronomy and Astrophysics, Peking University, Beijing 100871, People's Republic of China

³Department of Astronomy, Peking University, Beijing 100871, People's Republic of China

⁴Laboratory for Atmospheric and Space Physics, University of Colorado Boulder, Boulder, CO 80303, USA

ABSTRACT

We present the results of the first high-sensitivity NUV (1800 to 3200 Å) survey of FU Ori objects, using the *Hubble Space Telescope* (HST) STIS spectrograph. We compare new low resolution spectra for 6 sources with predictions from accretion disk models and find that all show emission in excess of the disk model spectrum. The physical properties of the NUV emission excess are very consistent among the sample, with a mean luminosity of $10^{-1.11\pm0.4}~L_{\odot}$ and temperature of $16400\pm2600~{\rm K}$ – despite spanning 0.9 dex in M_* , 1.3 dex in \dot{M} , and 0.7 dex in $L_{\rm acc}$. We use the spectra to conclusively rule out the existence of a hot boundary layer in FU Ori accretion disks. We then discuss the source of the excess emission in the context of recent simulations of FU Ori outbursts and boundary layer accretion. The UV spectra also show the often-seen C II] 2326 Å multiplet and Mg II 2796/2803 Å doublet, as well as the unusual Fe II] 2507/2509 Å doublet, a feature that is not seen in the existing UV spectra of other young stellar objects. We measure and compare the luminosities of these lines in outbursting with those in non-outbursting objects.

1. INTRODUCTION

There is class of young stellar objects (YSOs) called FU Ori objects, or FUOrs (Herbig 1977), which are observed to undergo eruptive episodes during which they accrete mass at rates up to 10,000 times greater than typical YSOs (Hartmann & Kenyon 1996). These accretion-driven outbursts can last for several decades, with some appearing to have been in outburst for well over 100 years (e.g., V883 Ori and RNO 54, Strom & Strom 1993; Hillenbrand et al. 2023). The class is named for FU Ori, which underwent a $\Delta V = 4$ magnitudes outburst in 1937 (Wachmann 1954) and has remained at nearly its peak brightness for the past 87 years. Since the start of the FU Ori outburst, approximately 40 FUOrs have been found (Connelley & Reipurth 2018, Contreras-Pena et al. 2025, in prep). The enormous mass accretion rates of FUOrs $(10^{-5} - 10^{-4} M_{\odot} \text{ yr}^{-1})$ radically alter the geometry of the accretion of material from the disk onto the star.

In non-outbursting YSOs, the classical T Tauri stars (CTTSs), the accretion geometry is that of magnetospheric accretion (Uchida & Shibata 1984). As material flows toward the star in the inner disk, it eventually meets an opposing pressure from the strong stellar magnetic field, which is stronger nearer the star. There the magnetic field energy density becomes comparable with the ram pressure of the inflowing material and the charged matter is lifted along the stellar magnetic field lines and deposited on the surface of the star (e.g., Zhu et al. 2024). The mass flow reaches the

star at freefall velocities (300 – 400 km s⁻¹) and creates a shock buried in the stellar photosphere. The shock-heated photospheric material at the location of the accretion column emits brightly at ultraviolet (UV) and blue visible wavelengths (Calvet & Gullbring 1998; Hartmann et al. 2016; Pittman et al. 2022). The UV spectra of CTTSs are thus typically dominated by accretion emission, rather than emission from the photosphere of the star.

In FUOrs, by contrast, when the disk undergoes an instability that dramatically increases the accretion rate, \dot{M} , the pressure balance is disrupted. For sufficiently high \dot{M} , the magnetosphere is overwhelmed by the accretion flow and the disk engulfs the star. The disk material accretes directly onto the stellar surface modulated by a boundary layer. The boundary layer itself has been theorized to be a region dominated by shear heating as the disk material in Keplerian rotation slows to the rotation rate of the central star (Popham et al. 1993). Models of the shear heated boundary layer predict a high maximum temperature, $T_{\rm max}$, of the disk at radii approaching the stellar radius, R_* (Popham et al. 1996). This high temperature shear-heated component should produce as a bright UV spectrum.

The accretion disk itself can reach temperatures of 7,000 – 8,500 K (Welty et al. 1992; Kenyon et al. 1989; Hartmann & Kenyon 1996; Carvalho et al. 2023b) and is thus intrinsically UV-bright. The extreme luminosity of the accretion disk and its high maximum temperature have thus far made detection of any UV excess relative to the disk challenging. Identifying

a UV excess requires going bluer than 3500-4500 Å, which is where the hottest components of the disk are brightest. Unfortunately, FUOrs are typically highly extincted (Connelley & Reipurth 2018) and appear quite faint in the UV. Altogether, detecting the predicted boundary layer excess would require high sensitivity FUV and NUV spectra.

We recently completed a Hubble Space Telescope (HST) survey aimed at detecting this predicted UV excess. We targeted 6 FUOrs that had previous U or B band measurements bright enough to ensure they would be detected in the NUV, and obtained low resolution spectra spanning 1800-5500~Å. We also sought a high resolution, deep spectrum of FU Ori in the FUV, in order to fully characterize the disk spectrum and any potential boundary layer excess emission at the disk-star interface.

In Carvalho et al. (2024c, hereafter C24), we published the finding that the FUV spectrum of FU Ori shows clear excess UV emission but its continuum shape and effective temperature are inconsistent with previous shear-heating models. We found that the continuum was instead more consistent with a magnetic heating or surface accretion shock origin.

In this article we present the UV spectra of the six FUOrs in our survey, including a re-discussion of FU Ori. All six objects have UV emission in excess of the viscous accretion disk. The luminosity of the excess component is correlated with the system luminosity, indicating the UV excess emission mechanism is related to accretion outburst itself. We also discuss the emission lines in the NUV spectra.

2. DATA

We obtained visible and NUV spectra of 6 FUOrs: FU Ori, V1057 Cyg, V1515 Cyg, V960 Mon, HBC 722, and BBW 76 as part of the Guest Observer (GO) program 17176 $^{\rm l}$. The sample was selected as the most blue/UV bright FU Ori objects known in 2022 (B<16 mag). The spectra were taken with the Hubble Space Telescope (HST) Space Telescope Imaging Spectrograph (STIS) using the $52''\times2''$ arcsec slit in 2 grating settings: G230L (NUV-MAMA) and G430L. An observation log is provided in Table 1.

The spectra cover the wavelength range 1800 Å to 5500 Å at a spectral resolution of $R \equiv \lambda/\Delta\lambda \sim 600$. The signal-to-noise (SNR) ratio per pixel varies depending on the brightness of the source. In order to improve the SNR of the spectra at the bluest wavelengths, we bin the G230L spectra in 30 Å increments, masking out the bright emission features at 2326 Å, 2505 Å, and 2800 Å. The three faintest objects in the sample, V1057 Cyg, BBW 76, and HBC 722, have very little

Table 1. HST/STIS Observations Log

Target	Date	Obs Time (s)	Grating	Wavelengths (Å)	
FU Ori	2023-10-08	1381	G230L	1580 - 3160	
	2023-10-08	45	G430L	2900 - 5700	
V1057 Cyg	2023-04-05	1886	G230L	1580 - 3160	
	2023-04-05	2818	G230L	1580 - 3160	
	2023-04-05	150	G430L	2900 - 5700	
V1515 Cyg	2025-01-01	1812	G230L	1580 - 3160	
	2025-01-01	2796	G230L	1580 - 3160	
	2025-01-01	150	G430L	2900 - 5700	
HBC 722	2023-08-27	1856	G230L	1580 - 3160	
	2023-08-27	180	G430L	2900 - 5700	
BBW 76	2024-02-15	1848	G230L	1580 - 3160	
	2024-02-15	2760	G230L	1580 - 3160	
	2024-02-15	130	G430L	2900 - 5700	
V960 Mon	2024-09-26	130	G230L	1580 - 3160	
	2024-09-26	1810	G230L	1580 - 3160	
	2024-09-26	2722	G430L	2900 - 5700	

flux to the blue of 2300 Å, as can be seen in the 2D spectra presented in Appendix A.

For our fainter objects, we consider the source detected if the peak of the spectral trace is $3\times$ the noise value in a given wavelength bin (see Appendix A for details). V1057 Cyg, BBW 76, and HBC 722 are not detected blueward of 2300 Å, 2000 Å, and 2300 Å, respectively, so for those objects we also computed 3σ upper limits on the flux in those wavelength bins. The upper limits are derived from the dark count level, cts_d , in each observation². We assume that the uncertainty is Poisson-distributed and thus $\sigma_d = \sqrt{cts_d}$. We then converted σ_d to an effective flux level using the response function of the detector. The spectra and upper limits are all shown in Figure 1.

3. MODELING THE SPECTRA

We model the NUV spectra with a two component model comprising a thin, viscously heated accretion disk and a single blackbody. We fit the two components generally following the same procedure described in C24, which we will summarize below.

The choice of extinction curve cannot be neglected in the analysis of UV data. The assumed shape of the 2175 Å fea-

¹ The data can be accessed at the Mikulski Archive for Space Telescopes (MAST) via doi: 10.17909/tpk0-8h65.

² The average dark counts subtracted per pixel from the image during processing is given in the x1d file header under the header key MEANDARK. We multiply this by the extraction region size, which is saved under the header key EXTRSIZE. This yields the total dark counts contributing to the uncertainty along the extraced object trace.

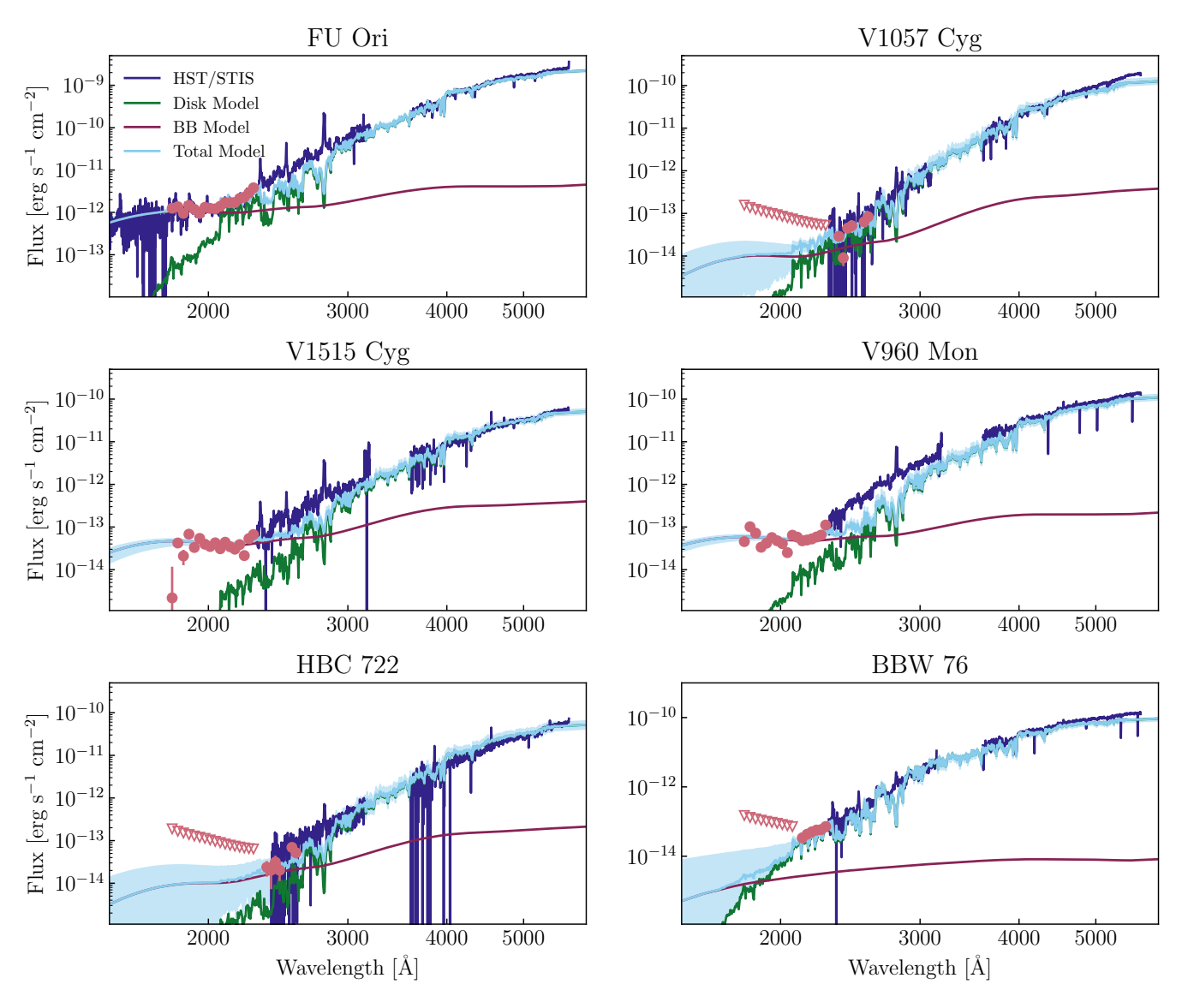


Figure 1. The G230L and G430L spectra for each of our objects (dark blue), along with the disk (green) and disk + UV excess (light blue) models for each of the FUOrs in the survey. The shaded regions show the range of the 16th and 84th percentile models from the MCMC samples. The blackbody component in each panel (maroon) matches the flux level of the binned continuum points (salmon) blueward of 2300 Å. The flux upper limits for V1057 Cyg, HBC 722, and BBW 76 are shown as empty triangles.

ture can significantly impact continuum shape of dereddened spectra. As in C24, we adopt the extinction curve from Whittet et al. (2004), which has been demonstrated to be more appropriate for the interstellar environment surrounding YSOs. The extinction curve contains two important features: a weak 2175 Å "bump" and a total-to-selective reddening factor, or R_V , of 3.63 (greater than the typically adopted galactic average from Cardelli et al. 1989). Recent extensive work aimed at measuring R_V along several Milky Way sightlines indicates that R_V values that are greater than the galactic average are found in dense environments near star-forming regions, and that R_V can reach 3.5 – 3.7 in the densest regions probed by the study (Zhang & Green 2025). For sources with suffi-

cient SNR at 2100 Å (FU Ori, V1515 Cyg, and V960 Mon, see Figure 1), the spectrum does not show the strong 2170 Å absorption feature predicted by the often-used Cardelli et al. (1989) or Fitzpatrick (1999) extinction laws.

3.1. The accretion disk component

The accretion disk model is the same that we successfully applied to model the spectra of FUOrs and is described in detail in Carvalho et al. (2023a) and Carvalho et al. (2024b). The primary assumption of the model is that the radial temperature profile of inner disk, $T_{\rm eff}(r)$, near the star can be described using the Shakura & Sunyaev (1973) α disk pre-

scription,

$$T_{\text{eff}}^4(r) = \frac{3GM_*\dot{M}}{8\pi\sigma_{\text{SB}}r^3} \left(1 - \sqrt{\frac{R_{\text{inner}}}{r}}\right),\tag{1}$$

where M_* is the stellar mass, \dot{M} is the disk-to-star mass accretion rate, $R_{\rm inner}$ is the innermost boundary of the disk, G is the universal gravitational constant, and $\sigma_{\rm SB}$ is the Stefan-Boltzmann constant. We modify the temperature profile so that $T_{\rm eff}(r < \frac{49}{36}R_{\rm inner}) = T_{\rm eff}(\frac{49}{36}R_{\rm inner}) \equiv T_{\rm max}$, following (Kenyon et al. 1988). This modification has been rigorously tested and upheld as an accurate description of the observed spectrum in both simulations (Zhu et al. 2020) and observations in the visible range (Rodriguez & Hillenbrand 2022; Liu et al. 2022) and the UV (C24).

For each of the objects in the sample, the disk model parameters we use are presented in Table 2. The disk model component for each object is shown in light blue in Figure 1. In the case of FU Ori, we adopted the best-fit parameters we found in C24. For HBC 722, we adopted the M_{\ast} and $R_{\rm inner}$ from Carvalho et al. (2024b) and scaled the \dot{M} downward to account for slightly fainter source brightness when the STIS spectrum was taken. For V960 Mon, we followed the prescription from Carvalho et al. (2023b) in order to scale the \dot{M} and $R_{\rm inner}$ in the model spectrum from the 2017 epoch to the 2023 epoch of the STIS observation.

The remaining three objects, BBW 76, V1515 Cyg, and V1057 Cyg required new model fits. The details of the fits are given in Carvalho (2026). We follow the general disk fitting procedure we have applied successfully to the other FUOrs. For these three objects, the free parameters we fit in the disk model are M_* , \dot{M} , $R_{\rm inner}$, i, and A_V . The SEDs we fit are combinations of the near-infrared (NIR) spectra from Connelley & Reipurth (2018) and the STIS G430L spectra, scaled to the flux of each target in 2015, when the NIR spectra were taken. We also use rotational broadening of lines in high resolution spectra to constrain the maximum Keplerian velocity in the disk (shown in Carvalho 2026).

3.2. The excess blackbody component

As can be seen in Figure 1, the disk model alone is insufficient to match the NUV continuum emission in all of the sources. The upper panel of Figure 2 shows the excess is stronger toward bluer wavelengths, with the observed flux diverging rapidly from the disk model flux for $\lambda < 2200$ Å.

In order to model the excess UV emission, we use a singletemperature blackbody, which we showed in C24 accurately matches the FUV and NUV excess emission in FU Ori. The blackbody component model is given by

$$F_{\lambda} = \pi B_{\lambda}(T_{\rm BB}) \left(\frac{R_{\rm BB}}{d}\right)^2,$$
 (2)

where d is the distance to the source, $R_{\rm BB}$ is the effective radius of the emission region, and $T_{\rm BB}$ is the effective temperature of the blackbody, B_{λ} . We treat the emission as a disk projected in the plane of the sky, since we do not know its true geometry and to maintain consistency with the assumption in C24. We assume that the A_V to the UV emission is the same as that of the system, reported in Table 2. We discuss the validity of this assumption in Section 5.

For the sources with the highest signal-to-noise spectra (FU Ori, V1515 Cyg, and V960 Mon), we apply the model to the binned continuum points with $\lambda < 2300$ Å, as this is where the excess relative to the disk model is strongest and where there are few bright emission lines contributing to the continuum bins. For the fainter sources (V1057 Cyg, BBW 76, and HBC 722), we use the bluest wavelength bins in which they are detected, according to the detection criteria in Section 2. The wavelength ranges used for the fits are reported in Table 3.

We then fit the three-parameter model using the log-likelihood based Markov-Chain Monte Carlo nested sampling code dynesty (Speagle 2020). The third parameter we vary in our model is A_V . This enables us to account for impact of A_V uncertainty on the UV excess luminosity measurements. We sample the A_V values at each iteration from a Gaussian distribution centered on the disk model best-fit and a standard deviation equal to the $\sigma(A_V)$, both of which are given in Table 2 for each source. The median values from the posterior distributions, which we adopt as our best-fits, are reported in Table 3. For all of the sources, the median A_V in the posterior distributions was within 1σ of the injected mean value, as expected, so we do not report these in Table 3. The posterior distributions themselves are shown in Appendix B.

Due to the lack of signal for $\lambda < 1800$ Å in our spectra, we are unable to adequately constrain the maximum possible temperature of the blackbody. The greatest temperature we allow the walkers to explore is 20000 K, since greater temperatures were ruled out in by the FU Ori FUV spectrum. However, we confidently rule out temperatures below 7,000 K for all of our objects. For FU Ori, V960 Mon, and V1515 Cyg, $T_{\rm BB} > 12000$ K is strongly preferred. The posterior distributions follow the expected $R_{\rm BB}^2 \propto T_{\rm eff}^4$ for a fixed luminosity, enabling us to compute the luminosity of the UV excess as $L_{\rm excess} = \pi R_{\rm BB}^2 \sigma_{\rm SB} T_{\rm BB}^4$. We report the luminosities in Table 3 and discuss them in Section 3.3.

3.3. Results of the blackbody fits and UV excess component properties

Our spectra of five additional FUOrs confirm the observed properties of the UV excess in FU Ori itself. In particular, the excess components all have temperatures in excess of 12,000 K and filling factors of $< 10^{-3}$ of the stellar surface (Table 3).

Table 2. The adopted disk model parameters for each object in the sample. Note that parameters like \dot{M} , $R_{\rm inner}$ and the emergent $T_{\rm max}$ and $L_{\rm acc}$ all vary over the course of an outburst. The parameters reported in this Table reflect the state of each system at the time of observation. We show only the uncertainty on A_V here because we incorporated it into our MCMC blackbody fits to account for its large effect on UV luminosity.

	M	$\log \dot{M}$	$R_{\rm inner}$	inc	A_V	$\sigma(A_V)$	d^a	$T_{\rm max}$	$L_{ m acc} b$
Object	(M_{\odot})	$(M_{\odot} { m yr}^{-1})$	(R_{\odot})	(deg)	(mag)	(mag)	(pc)	(K)	(L_{\odot})
FU Ori	0.60	-4.49	3.52	35	1.50	0.10	404	5970	86
V1057 Cyg	1.61	-5.32	2.67	8	2.72	0.20	795	5858	46
V1515 Cyg	1.0	-5.68	1.82	2	2.23	0.16	960	5609	89
V960 Mon	0.59	-4.96	2.69	15	1.60	0.2	1120.0	5550	38
HBC 722	0.20	-4.18	3.65	79	2.30	0.24	745.0	5840	85
BBW 76	0.20	-5.38	1.41	21	0.43	0.14	1040.0	5398	9

^aThe distance references are as follows: FU Ori (Kounkel et al. 2018; Roychowdhury & Hillenbrand 2024); V1057 Cyg (Szabó et al. 2021); V1515 Cyg (Szabó et al. 2022); V960 Mon (Kuhn & Hillenbrand 2019); HBC 722 (Kuhn & Hillenbrand 2019); BBW 76 (Gaia Collaboration et al. 2023).

In our sample of 6 objects, the mean $L_{\rm excess}=0.04\pm0.02\,L_{\odot}$, excluding BBW 76, which shows almost no excess. The mean temperature $T_{\rm BB}=16,200\pm2,400~{\rm K}$ and size $R_{\rm BB}=0.05\pm0.02~R_{\odot}$ are consistent with what we found for the UV excess of FU Ori using continuum regions of a COS FUV spectrum (C24).

As can be seen in the lower panel of Figure 2, the $L_{\rm excess}$ values show little dependence on the $L_{\rm acc}$ of the system. There is also no correlation between $L_{\rm excess}$ and $\dot{M},~M_*,~R_{\rm inner},~{\rm or}~i$. The uniformity of the UV excess across the sample (with BBW 76 as a notable outlier) may have provide hints as to its origin and its relation to boundary layer accretion in general. We discuss the potential emission source in detail in Section 5.3 and the extremely weak excess in BBW 76 in Section 5.4.

4. NUV EMISSION LINES

The NUV spectra of the FUOrs show 3 prominent emission features: the often-seen C II] 2326 Å multiplet and Mg II 2796/2803 Å doublet, as well as the unusual Fe II] 2507/2509 Å doublet. We discuss each of these features in detail below.

In order to understand the differences between these emission lines in FUOrs and their counterparts in CTTSs, we compute the line luminosities for each feature and discuss the measurements in the following Section. The CTTS we select for comparison is BP Tau. We justify the choice of BP Tau as a representative CTTS in Appendix C. We measure its line luminosities in the STIS G230L spectrum obtained in 2002 in the HST GO program 9081 (PI: N. Calvet; Kravtsova

& Lamzin 2003), which was accessed through MAST. We adopt a distance of 131 pc (Gaia Collaboration et al. 2023) and an $A_V=0.41$ mag to the source (Herczeg & Hillenbrand 2014).

The line fluxes were measured from the dereddened spectra, which were extinction-corrected using the A_V values reported in Table 2 and the Whittet et al. (2004) extinction law. We then fit a pseudocontinuum near the line using the specutils function fit_continuum and compute the line flux via direct integration. The integration limits for each lines are: 2310-2340~Å (C II]), 2503-2515~Å (Fe II]), and 2780-2820~Å (Mg II). The flux is then converted to a luminosity using the source distances in Table 3. The luminosity measurements are shown in Figure 4.

4.1. The Mg II doublet

The brightest feature in the NUV spectra of all 6 objects is the Mg II 2796/2803 Å doublet. Although doublet luminosity has been shown to correlate with the accretion luminosity of CTTSs, it can display P Cygni profiles typical of lines that trace outflows and has been seen in non-accreting, but magnetically active, YSO spectra (Ingleby et al. 2013; Xu et al. 2021). The high resolution 2001 HST/STIS E230M spectrum of FU Ori also reveals strong outflow absorption in the Mg II doublet, as both features are in clear P Cygni profiles (Kravtsova et al. 2007).

Despite the unknown degree of outflow absorption in the profiles, we measure and report the doublet luminosity for each object. The high resolution E230M spectrum of the FU Ori (Kravtsova et al. 2007) shows that the deep blue-shifted absorption removes approximately half of the flux

^b This accretion luminosity is *not* the bolometric luminosity of the source.

 Table 3. The best-fit blackbody component parameters and NUV emission line luminosities for each object in the sample.

	Fit Range	${ m log}R_{ m BB}$	$T_{ m BB}$	$\log(L_{ m excess})$	$L_{ m MgII}$	$L_{\mathrm{CII}]}$	$L_{ m FeII]}$
Object	(Å)	(R_{\odot})	(K)	(L_{\odot})	$(10^{-3}~L_\odot)$	$(10^{-3} L_{\odot})$	$(10^{-3} L_{\odot})$
FU Ori ^a	1800 - 2300	-1.3 ± 0.2	$16,000 \pm 1,000$	-1.06 ± 0.01	78.9 ± 0.3	7.0 ± 0.1	7.0 ± 0.1
V1057 Cyg	2350 - 2500	-1.1 ± 0.4	$13,200 \pm 5,000$	-1.08 ± 0.35	26.1 ± 2.5	9.9 ± 0.6	3.8 ± 0.2
V1515 Cyg	1800 - 2300	-1.2 ± 0.3	$16,400 \pm 3,000$	-1.06 ± 0.18	31.4 ± 4.7	5.3 ± 0.2	4.5 ± 0.7
V960 Mon	1800 - 2300	-1.4 ± 0.2	$18,000 \pm 2,000$	-1.32 ± 0.16	23.4 ± 3.5	1.1 ± 0.3	0.9 ± 0.5
HBC 722	2350 - 2500	-1.3 ± 0.6	$12,200 \pm 5,000$	-1.57 ± 0.55	5.20 ± 0.4	< 9.0	0.34 ± 0.01
BBW 76	2100 - 2300	-2.0 ± 0.7	$8,500 \pm 5,000$	-3.72 ± 1.28	0.38 ± 0.17	0.01 ± 0.01	0.1 ± 0.01
Average ^b	• • •	-1.28 ± 0.4	$16,400 \pm 2,600$	-1.11 ± 0.40	• • •	• • •	

^aSince the excess $T_{\rm BB}$ and $R_{\rm BB}$ are well constrained for FU Ori in C24, we adopt those values in this Table.

from the total line emission. Therefore, our reported luminosities should be considered lower limits on the intrinsic Mg II doublet luminosity of FUOrs.

Visually, the Mg II line strengths look similar across the sample, with the exception of BBW 76 and V1057 Cyg. In these two objects, the Mg II emission is much weaker relative to the other two emission features, an effect that is quantified in the ratios plotted in Figure 4. We discuss the potential implications of this in Section 5.

4.2. The C II] complex at 2326 Å

The C II] emission feature at 2326 Å is in fact a blend of multiplets from three species: C II], Si II], and Fe II]. The features in the wavelength range over which we measure line flux that contribute most strongly to the line are: C II] 2324.21, 2325.4, 2326.11, 2327.64, and 2328.83, Si II] 2329.23, and 2335.12/2335.32, and Fe II] 2328.11. In the STIS E230M spectrum of FU Ori, the Si II] 2335.12/2335.32 doublet has a blue-shifted absorption/red-shifted emission P Cygni profile. The emission from the Fe II] features in the region is also mildly red-shifted, suggesting they may be in P Cygni profiles as well. This indicates that at least the Fe II] and Si II] features trace an outflow in the system.

Looking closely at the C II] multiplet in the STIS E230M spectrum of FU Ori reveals that the lines are unlikely to arise from an optically thin plasma in collisional equilibrium. In CTTSs, this assumption has enabled the estimation of temperature and number density of the line-emitting material based on flux ratios of lines in this complex (López-Martínez & Gómez de Castro 2014). We test this assumption in FU Ori using line emissivities from the CHIANTI database. Over a broad range of electron densities ($n_e=10^2-10^{15}~{\rm cm}^{-3}$) and temperatures ($T_e=10^4-10^6~{\rm cm}^{-3}$), the ratio of C II] 2325.4/2326.11 intensities is at most 0.2-0.3. In the FU

Ori E230M spectrum, the ratio is 0.74, indicating the level population of the multiplet is in disequilibrium.

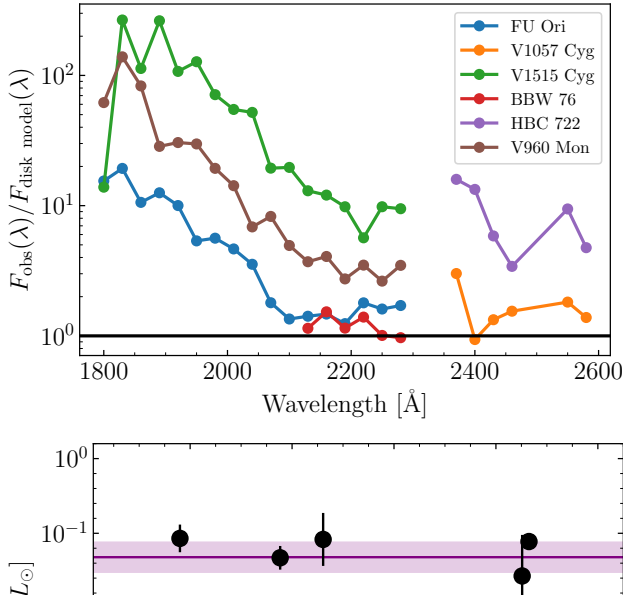
Although in CTTSs the C II] 2326 Å luminosity is a reliable tracer and diagnostic of accretion, its luminosity in FUOrs does not follow the same scaling. If we apply the Ingleby et al. (2013) relation found for CTTSs, $\log L_{\rm acc} = 1.1 \log(L_{\rm CII]}) + 2.7$, the $L_{\rm acc}$ values for the FUOrs are underpredicted by factors of 40-160. There is some mild correlation between the $L_{\rm CII]}$ and $L_{\rm acc}$ values, however, which can be fit by $\log(L_{\rm acc}) = 1.66 \log(L_{\rm CII]}) - 5.16$ (omitting the HBC 722 upper bound in the fit). The best fit is shown in Figure 4.

4.3. The Fe II doublet and its origin

There is a strong feature at 2508 that we identified as the Fe II] 2507/2509 doublet in the spectrum of FU Ori (C24). The luminosity of the line closely matches the luminosity of the C II] feature in all of the sources, even matching the $L_{\rm CII}$ upper limit in HBC 722. This indicates that the feature may also correlate with the $L_{\rm acc}$ of FUOrs (except HBC 722). However, as we discuss below, the origin of the feature is not well-understood.

The presence of the Fe II] 2507/2509 doublet in the spectra of FUOrs is surprising. It is not seen at all in the spectra of other accreting YSOs, but has been observed in spectra of evolved systems like symbiotic binaries, η Carinae, and chromospherically-active giants (Johansson & Hamann 1993; de la Reza 2025), indicating it may be diagnostic of boundary layer accretion. The feature is not expected to appear as brightly as we see it in the FUOr spectra in isolation. For an optically thin plasma in local thermodynamic equilibrium, there are several Fe II emission lines around 2495-2520 Å that should be as bright as or brighter than the 2507/2509 doublet (Dere et al. 1997; Del Zanna et al. 2021). However, the high resolution STIS E230M spectrum

^bExcluding BBW 76.



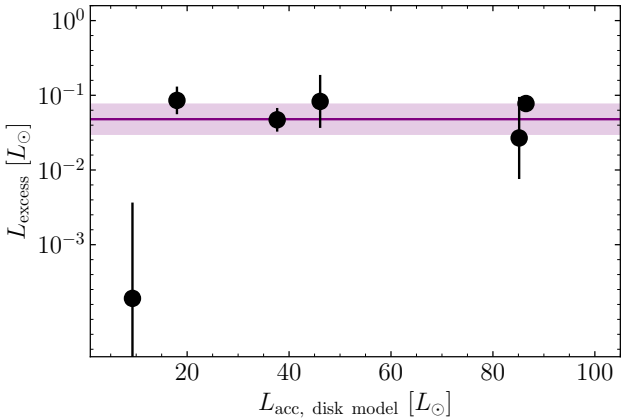


Figure 2. Upper Panel: The ratio of the observed binned STIS spectra used to fit the blackbody excess model and the disk models binned to the same wavelength sampling. Notice that for all the FUOrs in the sample, the NUV flux is at least $2\times$ as bright as the disk model predicts at 2200 Å and for many the flux ratio is >10 (for HBC 722 and V1057 Cyg, this is true at 2400 Å, despite the lack of data at 2200 Å). Lower Panel: The $L_{\rm excess}$ measurements for each of the FUOrs compared with their disk-model-derived $L_{\rm acc}$. The error bars on each point are given by the 1σ ranges of their posterior distributions. The mean and standard deviation on the UV excess luminosities (excluding BBW 76) are marked by the purple line and shading, respectively.

of FU Ori confirms that the doublet is much brighter than any nearby Fe II features (Kravtsova et al. 2007).

The strength of the doublet relative to other Fe II features in the same wavelength range is attributed to fluorescence via one of two proposed mechanisms: photoexcitation by accidental resonance or photoexcitation by continuum resonance (termed PAR or PCR, respectively, Johansson & Hamann 1993). Both mechanisms rely on photons in the 1000-1300 Å wavelength range to pump Fe II transitions that populate energy levels around 11-12 eV, which eventually cascade downward and through the 2507/2509 lines (Johansson & Hamann

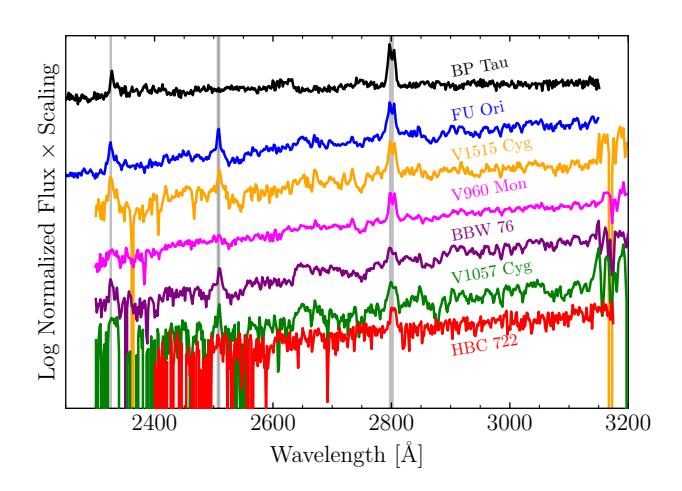


Figure 3. The STIS G230L spectra of the 6 FUOrs and the CTTS BP Tau for reference. The spectra are sorted top-to-bottom in order of decreasing signal-to-noise. The grey vertical lines mark the locations of the emission features discussed in Section 4.

1993)³. While it is beyond the scope of this paper to model the emission of this doublet in detail, we did investigate the PAR/PCR mechanisms discussed in Johansson & Hamann (1993) and their plausibility in FUOrs.

The PAR mechanism relies on the coincidence between the wavelength of an existing emission line and that of a transition in another species. In the case of the 2507/2509 doublet, Johansson & Hamann (1993) propose that very redshifted Ly α might excite electrons via transitions at 1217.85 Å and 1218.21 Å, which would require Ly α emission reaching $500-600~{\rm km~s^{-1}}$. Alternatively, $-70~{\rm km~s^{-1}}$ emission by the O V 1218.5 Å line could also excite the same transition. In C24, we found high velocity red-shifted Ly α in the high resolution FUV spectrum of FU Ori, as well as blue-shifted emission from O V at 1371 Å with a velocity of $-80~{\rm km~s^{-1}}$. Though this suggests Ly α emission as a promising PAR source, CTTSs have extremely bright Ly α at velocities of $500-600~{\rm km~s^{-1}}$ (Arulanantham et al. 2023) but do not show the Fe II doublet.

In the case of PCR, all that is necessary is bright continuum emission in the correct wavelength range to excite the desired transition. Johansson & Hamann (1993) propose that Fe II ground transitions around 1100-1115 Å can be excited by continuum emission. A clear signature of this excitation mechanism would be a series of absorption features in 1100-1115 Å wavelength range, though that may depend on the geometry of the absorbing material. There is also the case of the 1785 Å Fe II feature, which can result from PCR of ground transitions around 1270 Å (Hempe & Reimers 1982). While

 $^{^3}$ The specific transitions are identified by Johansson & Hamann (1993) as $5p^6F^\circ_{9/2}\to 4s~c^4F_{7/2}$ and $4p^4G^\circ_{9/2}\to 4s~c^4F_{7/2}$ for 2507 Å and 2509 Å, respectively.

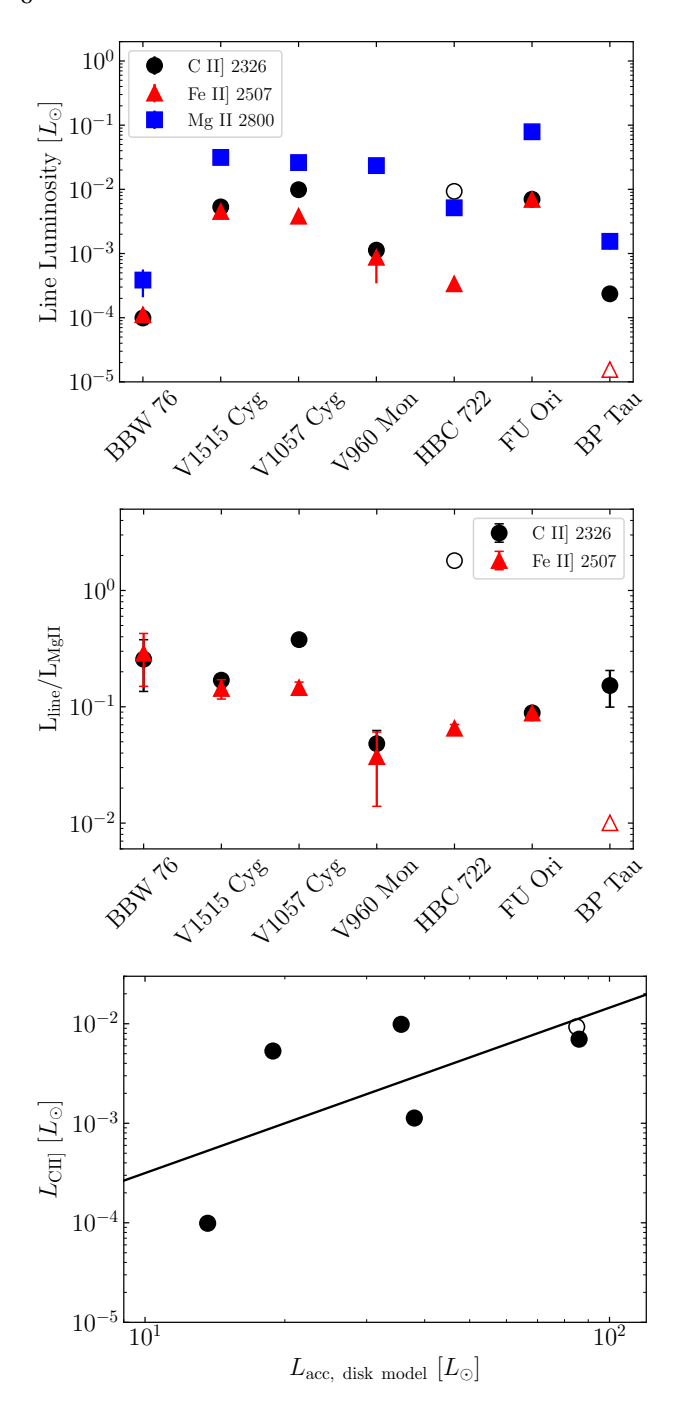


Figure 4. Top: The C II] (black circles), Fe II] (red triangles), and Mg II (blue squares) line luminosities for the FUOr sample and the CTTS BP Tau. Error bars are drawn but are smaller than the symbols for most measurements. The empty circle (triangle) for HBC 722 (BP Tau) represents the 3σ upper limit on the C II] (Fe II]) luminosity. The FUOrs are sorted left-to-right in order of increasing $L_{\rm acc}$. **Middle:** The same line C II] and Fe II] luminosities divided by the Mg II luminosities. **Bottom:** The $L_{\rm CII}$] measurements plotted against the $L_{\rm acc}$ for the FUOrs. The black line shows the best-fit relation described in Section 4.2.

the signal-to-noise ratio of the FUV spectrum of FU Ori is in-

sufficient to detect the predicted line absorption, PCR would explain the strength of the bright feature at 1785 Å seen in the FUV spectrum of FU Ori C24. Given the bright FUV continuum of FU Ori, which we showed extends beyond 1150 Å (C24), it is possible that PCR in the 1100 Å range could pump the upper transitions of the 2507/2509 doublet.

Both PAR and PCR can also produce fluorescent line emission at wavelengths around 9000 Å, but the lines would be significantly fainter than the accretion disk and therefore not observable in the spectra of FUOrs. Clearly identifying or ruling out PAR/PCR as the source of the transition pumping photons would require both careful modeling of this mechanism in FUOrs and a much more sensitive FUV spectrum of FU Ori.

5. DISCUSSION

In Section 3.3, we demonstrated that all six FUOrs in the sample possess excess UV continuum emission that reaches more than $10\times$ the disk model flux, as shown in Figure 2. We also found that the excess emission spans a narrow range of luminosities ($L_{\rm excess} \sim 0.04~L_{\odot}$), temperatures ($T_{\rm BB} \sim 12000-18000~{\rm K}$), and physical size ($R_{\rm BB} \sim 0.02-0.06~R_{\odot}$). Despite the 0.9 dex range in stellar mass and 1.2 dex range in mass accretion rate, the $L_{\rm excess}$ excess varies little across the sample. Here, we discuss the potential source of the emission in the context of the classical boundary layer accretion model for FUOrs and the exceptional case of the source BBW 76.

5.1. The UV Excess Emission in FUOrs compared with CTTSs

To contextualize the luminosity of the UV excess in FU Ori objects relative to other YSOs, we compare our measurements with the UV survey of CTTSs compiled by Yang et al. (2012). We restrict our comparison to the lower mass and lower luminosity subset of CTTSs ($L_{\rm acc} < 1~L_{\odot}$), since they better reflect the pre-outburst FUOrs in our survey.

Directly comparing the UV emission from both sets of objects is challenging due to the different accretion geometries in each. In CTTSs, for instance, a large fraction (10-50%) of the accretion luminosity is emitted at $2000<\lambda<3100$ Å (termed $L_{\rm space}$ in Pittman et al. 2025). Integrating our disk + blackbody models in the range $2000<\lambda<3100$ Å, we find a median $L_{\rm space}=10^{-1.7\pm0.4}~L_{\odot}$, which is only a bit smaller than $L_{\rm excess}$. Dividing by the $L_{\rm acc}$ values in Table 2, we obtain $L_{\rm space}/L_{\rm acc}=10^{-3.4\pm0.2}$. In other words, only a very small fraction of the total $L_{\rm acc}$ in FUOrs is emitted in the NUV, though the actual NUV luminosities themselves are high.

Comparing the luminosities of the CTTSs and FUOrs in the FUV is further complicated by the lack of FUV spectra in our survey (with the exception of FU Ori). Although we do not have FUV spectra for the other 5 objects in the sample, we can extrapolate the blackbodies into the FUV. The blackbodies have similar best-fit $T_{\rm BB}$ and $R_{\rm BB}$ to the FUV-derived best-fit values for FU Ori, indicating the FUV continuum emission in our sample is likely well-represented by these blackbody fits.

We then integrate the blackbodies in the range 1250-1700 Å, as was done to measure the $L_{\rm FUV}$ of CTTSs reported in Yang et al. (2012). The mean $L_{\rm FUV,FUOr}=0.012\pm0.007~L_{\odot}$ following this process. This is $7.5\times$ greater than the mean $L_{\rm FUV,CTTS}=0.0016\pm0.002L_{\odot}$ for the CTTSs in the Yang et al. (2012) with $L_{\rm acc}<1~L_{\odot}$. The true difference between the FUV continuum luminosities of the two samples is likely greater, since the FUV spectra of CTTSs are emission-line-dominated, with continuum emission matching the typical accretion shock models for $T_{\rm eff}=10^4~{\rm K}$ (France et al. 2011).

5.2. The Missing Boundary Layer in FUOrs

In the viscous accretion disk model applied to FUOrs (Lynden-Bell & Pringle 1974; Kenyon et al. 1988), only half of the viscous dissipation of gravitational energy $(GM_*\dot{M}/R_{\rm inner})$ is expected to be radiated by the disk itself. A key assumption is that as material approaches the star, it must decelerate from its large Keplerian rotation rate to the much slower stellar rotation rate. This requires dissipating the remaining half of the initial gravitational energy over a region known as the dynamical boundary layer.

If the energy dissipation mechanism in the dynamical boundary layer is viscosity, then the energy should be efficiently radiated away as the material is heated. The dynamical boundary layer would then have a luminosity as great as the accretion disk due to this extreme shear ($L_{\rm BL}=L_{\rm acc}$). In our survey, the median value of $L_{\rm excess}/L_{\rm acc}$ measured for the 6 FUOrs is $10^{-2.9\pm0.4}$, which is several orders of magnitude below what would be expected of a shear-heated boundary layer.

A potential solution is to assume that the boundary layer may be confined to latitudes near disk midplane and obscured from our view due to the surface accretion layer. Could the UV spectrum be reproduced by adopting a higher temperature ($T_{\rm BL} \sim 30,000$ K, Hartmann & Kenyon 1985) and luminosity ($L_{\rm BL} = 85~L_{\odot}$) for the boundary layer but obscuring it under some larger A_V ? We explored this using the FUV spectrum of FU Ori and found that even for large $T_{\rm BL}$, adopting $A_V > 2$ mag results in model spectra that underpredict the flux for $\lambda < 1600$ Å.

We note that the obscuring material is probably not dust, and thus A_V may not be an appropriate proxy for its absorption. However, if we were to instead model the gas absorption against the 30,000 K continuum, the absorption would be dominated by the bound-free transitions in metallic species

like C and Si, which have even greater continuous opacities than dust at FUV wavelengths (Travis & Matsushima 1968). We do not see these features in the FUV spectrum of FU Ori, but it is possible that the continuum sensitivity is insufficient to detect them. Perhaps future large UV/optical telescopes with greater senstivity will reveal these continuum features in the FUV spectra of FUOrs. In either case, for the large column densities necessary to diminish the observed $L_{\rm BL}/L_{\rm acc}$ by several orders of magnitude, the FUV continuum at $\lambda < 1600$ Å is severely underestimated.

The upper limit on extinction also places an upper limit of $0.6~L_{\odot}$ on the luminosity of an obscured boundary layer. It is therefore unlikely that the FUV continuum in FU Ori is due to a classical boundary layer obscured by disk material along the line of sight. Furthermore, (Popham et al. 1993) found that for the high accretion rates in FUOrs, the boundary layer should extend over as much as $0.2~R_{*}$, which is incompatible with the median $R_{\rm BB}=0.05~R_{\odot}$.

The uniformly low luminosity and small spatial scale of the UV excess in FUOrs is inconsistent with the classical models for a hot boundary layer. In C24, we also provide a more extensive discussion of other models for shear-heated boundary layers, both in the literature of YSOs and compact objects, and why the UV excess in FU Ori is inconsistent with those.

In short, the remaining gravitational energy of the gas near the stellar surface is not dissipated by heating the boundary layer. It is instead likely that the pressure support from the strong magnetic fields near the surface of the star slows the material as it approaches. The interacting disk and stellar fields in the boundary layer are capable of efficiently removing large amounts of angular momentum via Maxwell stresses (Takasao et al. 2025). The magnetic field is thus capable of slowing material down to the stellar rotation rate without strongly heating the gas.

5.3. The source of the UV continuum excess in FUOrs

As we established in Section 5.2, the UV excess emission in FUOrs does not arise from a classical hot boundary layer. What could the source of the excess be, then?

In CTTSs, the UV excess emission arises from the heated pre-shock and post-shock material in the photosphere (Calvet & Gullbring 1998; Hartmann et al. 2016). This material is expected to be 8,000-10,000 K, while the shock temperature is expected to be $\sim 9\times 10^5$ K due to the high free-fall velocities of matter flowing along the accretion funnel.

The picture we presented in C24 was that the FUV continuum in FU Ori is from a directly-observed accretion shock that is much cooler than that of CTTS systems. The velocity of material producing this shock is the surface accretion flow velocity at the disk-star interface, which is found to be $\sim 40\%$ of the Keplerian velocity near the star (Zhu et al. 2020). For most of our sources, the Keplerian velocity at

 $r=R_*$ is $160\pm20~{\rm km~s^{-1}}$, indicating a surface flow velocity of $v_{\rm surf}=64\pm8~{\rm km~s^{-1}}$. If we assume that the resulting shock is a strong shock, we estimate the shock temperature: $T_s=\frac{3}{16}\frac{\mu m_H}{k}v_{\rm surf}^2=45,500~{\rm K}$, where k is the Boltzmann constant, m_H the mass of the hydrogen atom, and μ the mean atomic weight, set to 0.5 here since the material is likely fully ionized. $T_s=45,500$ is much greater than the maximum $T_{\rm BB}$ in the sample.

If we assume that the the magnetic pressure support from the star/disk field at the boundary further slows the material (Takasao et al. 2025), we can adopt 40 km s $^{-1}$ as the inflow shock velocity and compute $T_s=17,300$ K, which is in better agreement with the $T_{\rm BB}$ values. The range of temperatures observed in the sample can then be reproduced by increasing or decreasing $v_{\rm surf}$ by just $5~{\rm km~s^{-1}},$ while the range of $v_{\rm Kep}(R_*)$ in our sample is more than $100~{\rm km~s^{-1}}.$ We observe a weak correlation between $T_{\rm BB}$ and $v_{\rm Kep}(R_*),$ supporting the idea that $v_s \propto v_{\rm Kep}(R_*)$ subject to some braking effect.

It is also conceivable that the magnetic deceleration of the surface flow may be more efficient in systems with greater $v_{\rm Kep}(R_*)$. The magnetic deceleration depends in part on the strength of the bundled fields near the stellar surface, which depend on the shear between the star and disk (Takasao et al. 2025). Systems with larger $v_{\rm Kep}(R_*)$ may thus have stronger fields at R_* and more effectively brake the more rapid flow. In this way the deceleration may regulate the accretion flow velocity to produce the narrow range of observed temperatures.

An alternative hypothesis is that the UV emission arises from material above the star that is heated by rapidly recurring magnetic reconnection events at the star-disk interface. These events are seen in simulations of boundary layer accretion and are proposed to be the energy source heating the material emitting soft X-rays in FUOrs (Takasao et al. 2025). This would also explain the high temperatures of the X-rays in FUOrs (Kuhn & Hillenbrand 2019), as well as the hour-to-hour variability of X-ray luminosity in FU Ori (Skinner et al. 2010). The UV emission may then be from material between the stellar surface and the hot corona above.

5.4. The strange case of BBW 76

A potential hint to the UV excess emission source lies in the outlier of our sample: BBW 76. We do detect the UV excess in the source, but it has an $L_{\rm excess}$ that is $13\times$ smaller than the median in the sample. Our upper limits on the flux blueward of 2000 Å also rule out the potential of a hotter or brighter component with $L_{\rm excess}>0.02~L_{\odot}$ (5× fainter than the rest of the sample), despite an accretion luminosity of $L_{\rm acc}=9~L_{\odot}$. Furthermore, BBW 76 has an NUV line emission spectrum that is distinct from the other FUOrs. The Mg II 2800 Å doublet is much less luminous than in the other

objects, even the CTTS BP Tau, and there is a strong continuum break at 2650 Å, which appears only weakly in the other objects.

While its large (relative to CTTSs) accretion luminosity confirms it is still in outburst, recent photometry from ASAS-SN and NEOWISE (Shappee et al. 2014; Mainzer et al. 2011; Hart et al. 2023) shows that BBW 76 has faded monotonically by more than $\Delta V=0.3$ mag (and more than 0.7 mag since 2002, Siwak et al. 2020) and $\Delta W1=0.8$ mag in 10 years, while a recent near-infrared spectrum of the source shows significant spectroscopic evolution in the past 5 years (private communication). It is possible that the source has entered an intermediate stage between boundary layer accretion and magnetospheric accretion, wherein the proximity of the inner disk to the central star still produces a bright disk-dominated visible range continuum.

A transition between boundary layer accretion and magnetospheric accretion could result in a rapid decline in the UV excess luminosity. In the shock case, once the magnetospheric funnel flows re-establish themselves, the disk and stellar fields will separate spatially, lowering the magnetic flux (and therefore magnetic pressure) near the location of the former boundary layer. The pressure support will no longer slow the surface accretion flow, enabling it to impact the photosphere at velocities more similar to the CTTS case, embedding the shock in the photosphere. The lower $T_{\rm BB}$ in BBW 76 implies we may be seeing the heated photosphere re-processing this buried shock, rather than the shock itself.

The magnetic reconnection events that may produce the excess rely on the interaction of the stellar and disk fields at the boundary layer (Takasao et al. 2025). Once again, as the magnetospheric accretion funnels re-establish themselves, the disk and stellar surface will be separated, lessening the frequency of reconnection events. The heating would diminish and the temperature and luminosity of the emission would decrease as the system evolves away from boundary layer accretion.

6. CONCLUSIONS

Our recent HST/STIS survey of FUOrs reveals that FUV continuum emission in excess of the viscous accretion disk is common. The typical properties of the FUV continuum in the sample are: $L_{\rm excess}=10^{-1.11\pm0.4}~L_{\odot},~T_{\rm BB}=16,400\pm2,600~{\rm K},$ and $R_{\rm BB}=0.05\pm0.04~R_{\odot}.$ The consistent luminosities, temperatures, and physical sizes of the emitting material indicate a common source for the emission in all FUOrs.

The NUV line emission from the sample is also bright, though not as bright as predicted by correlations between line and accretion luminosity in CTTSs. The presence of strong Fe II] 2507/2509 doublet emission relative to other Fe II features also imply that the physical conditions of the plasma

emitting the NUV lines differ significantly from those in the NUV emitting accretion flows of CTTSs.

Recent magnetohydrodynamical simulations of both the FU Ori system and boundary layer accretion in protostars support two potential origins for the UV continuum emission: a shock where the surface accretion flow impacts the stellar surface or material above the star heated by magnetic reconnection events at the star/disk interface. The comparison of the properties of the UV emission and physical properties $(M_*, \dot{M}, R_{\rm inner})$ of the sample do not highlight a preference for one mechanism over another.

More detailed study and modeling of the emission lines in the NUV spectra will help to establish whether they share a common origin with the UV continuum emission. A UVsensitive spectrograph on a future large space telescope will be critical for expanding the number of FUOrs with NUV and FUV spectroscopy beyond the 6 covered in this study.

Software: Astropy (Astropy Collaboration et al. 2013, 2018, 2022), NumPy (Harris et al. 2020)

REFERENCES

Arulanantham, N., Gronke, M., Fiorellino, E., et al. 2023, ApJ, 944, 185, doi: 10.3847/1538-4357/acaf70

Astropy Collaboration, Robitaille, T. P., Tollerud, E. J., et al. 2013, A&A, 558, A33, doi: 10.1051/0004-6361/201322068

Astropy Collaboration, Price-Whelan, A. M., Sipőcz, B. M., et al. 2018, AJ, 156, 123, doi: 10.3847/1538-3881/aabc4f

Astropy Collaboration, Price-Whelan, A. M., Lim, P. L., et al. 2022, ApJ, 935, 167, doi: 10.3847/1538-4357/ac7c74

Calvet, N., & Gullbring, E. 1998, ApJ, 509, 802, doi: 10.1086/306527

Cardelli, J. A., Clayton, G. C., & Mathis, J. S. 1989, ApJ, 345, 245, doi: 10.1086/167900

Carvalho, A. S. 2026, PhD thesis, doi: 10.7907/4E53-3N79

Carvalho, A. S., Herczeg, G. J., France, K., & Hillenbrand, L. A. 2024a, Research Notes of the American Astronomical Society, 8, 232, doi: 10.3847/2515-5172/ad7ba3

Carvalho, A. S., Hillenbrand, L., & Seebeck, J. 2023a, ApJ, 958, 140, doi: 10.3847/1538-4357/acff59

Carvalho, A. S., Hillenbrand, L., Seebeck, J., & Covey, K. 2024b, ApJ, 971, 44, doi: 10.3847/1538-4357/ad5286

Carvalho, A. S., Hillenbrand, L. A., France, K., & Herczeg, G. J. 2024c, ApJL, 973, L40, doi: 10.3847/2041-8213/ad74eb

Carvalho, A. S., Hillenbrand, L. A., Hambsch, F.-J., et al. 2023b, ApJ, 953, 86, doi: 10.3847/1538-4357/ace2cb

Connelley, M. S., & Reipurth, B. 2018, ApJ, 861, 145, doi: 10.3847/1538-4357/aaba7b

de la Reza, R. 2025, A&A, 693, A98,

doi: 10.1051/0004-6361/202451727

Del Zanna, G., Dere, K. P., Young, P. R., & Landi, E. 2021, ApJ, 909, 38, doi: 10.3847/1538-4357/abd8ce

Dere, K. P., Landi, E., Mason, H. E., Monsignori Fossi, B. C., & Young, P. R. 1997, A&AS, 125, 149, doi: 10.1051/aas:1997368

Fitzpatrick, E. L. 1999, PASP, 111, 63, doi: 10.1086/316293

Foreman-Mackey, D. 2016, The Journal of Open Source Software, 1, 24, doi: 10.21105/joss.00024

France, K., Yang, H., & Linsky, J. L. 2011, ApJ, 729, 7, doi: 10.1088/0004-637X/729/1/7

Gaia Collaboration, Vallenari, A., Brown, A. G. A., et al. 2023, A&A, 674, A1, doi: 10.1051/0004-6361/202243940

Harris, C. R., Millman, K. J., van der Walt, S. J., et al. 2020, Nature, 585, 357, doi: 10.1038/s41586-020-2649-2

Hart, K., Shappee, B. J., Hey, D., et al. 2023, arXiv e-prints, arXiv:2304.03791, doi: 10.48550/arXiv.2304.03791

Hartmann, L., Herczeg, G., & Calvet, N. 2016, ARA&A, 54, 135, doi: 10.1146/annurev-astro-081915-023347

Hartmann, L., & Kenyon, S. J. 1985, ApJ, 299, 462, doi: 10.1086/163713

Hartmann, L., & Kenyon, S. J. 1996, ARA&A, 34, 207, doi: 10.1146/annurev.astro.34.1.207

Hempe, K., & Reimers, D. 1982, A&A, 107, 36

Herbig, G. H. 1977, ApJ, 217, 693, doi: 10.1086/155615

Herczeg, G. J., & Hillenbrand, L. A. 2014, ApJ, 786, 97, doi: 10.1088/0004-637X/786/2/97

Hillenbrand, L. A., Carvalho, A. S., van Roestel, J., & De, K. 2023, ApJL, 958, L27, doi: 10.3847/2041-8213/ad0be0

Ingleby, L., Calvet, N., Herczeg, G., et al. 2013, ApJ, 767, 112, doi: 10.1088/0004-637X/767/2/112

Johansson, S., & Hamann, F. W. 1993, Physica Scripta Volume T, 47, 157, doi: 10.1088/0031-8949/1993/T47/025

Kenyon, S. J., Hartmann, L., & Hewett, R. 1988, ApJ, 325, 231, doi: 10.1086/165999

Kenyon, S. J., Hartmann, L., Imhoff, C. L., & Cassatella, A. 1989, ApJ, 344, 925, doi: 10.1086/167860

Kounkel, M., Covey, K., Suárez, G., et al. 2018, AJ, 156, 84, doi: 10.3847/1538-3881/aad1f1

Kravtsova, A. S., & Lamzin, S. A. 2003, Astronomy Letters, 29, 612, doi: 10.1134/1.1607499

Kravtsova, A. S., Lamzin, S. A., Errico, L., & Vittone, A. 2007, Astronomy Letters, 33, 755, doi: 10.1134/S1063773707110060

Kuhn, M. A., & Hillenbrand, L. A. 2019, ApJ, 883, 117, doi: 10.3847/1538-4357/ab3a3f

Liu, H., Herczeg, G. J., Johnstone, D., et al. 2022, ApJ, 936, 152, doi: 10.3847/1538-4357/ac84d2

- López-Martínez, F., & Gómez de Castro, A. I. 2014, MNRAS, 442, 2951, doi: 10.1093/mnras/stu1045
- Lynden-Bell, D., & Pringle, J. E. 1974, MNRAS, 168, 603, doi: 10.1093/mnras/168.3.603
- Mainzer, A., Bauer, J., Grav, T., et al. 2011, ApJ, 731, 53, doi: 10.1088/0004-637X/731/1/53
- Manara, C. F., Ansdell, M., Rosotti, G. P., et al. 2023, in
 Astronomical Society of the Pacific Conference Series, Vol. 534,
 Protostars and Planets VII, ed. S. Inutsuka, Y. Aikawa, T. Muto,
 K. Tomida, & M. Tamura, 539, doi: 10.48550/arXiv.2203.09930
- Pittman, C. V., Espaillat, C. C., Robinson, C. E., et al. 2022, AJ, 164, 201, doi: 10.3847/1538-3881/ac898d
- 2025, arXiv e-prints, arXiv:2507.01162, doi: 10.48550/arXiv.2507.01162
- Popham, R., Kenyon, S., Hartmann, L., & Narayan, R. 1996, ApJ, 473, 422, doi: 10.1086/178155
- Popham, R., Narayan, R., Hartmann, L., & Kenyon, S. 1993, ApJL, 415, L127, doi: 10.1086/187049
- Rodriguez, A. C., & Hillenbrand, L. A. 2022, ApJ, 927, 144, doi: 10.3847/1538-4357/ac496b
- Roman-Duval, J., Fischer, W. J., Fullerton, A. W., et al. 2025, ApJ, 985, 109, doi: 10.3847/1538-4357/adc45b
- Roychowdhury, T., & Hillenbrand, L. A. 2024, Research Notes of the American Astronomical Society, 8, 171, doi: 10.3847/2515-5172/ad5a9c
- Shakura, N. I., & Sunyaev, R. A. 1973, A&A, 24, 337
- Shappee, B. J., Prieto, J. L., Grupe, D., et al. 2014, ApJ, 788, 48, doi: 10.1088/0004-637X/788/1/48
- Siwak, M., Ogłoza, W., & Krzesiński, J. 2020, A&A, 644, A135, doi: 10.1051/0004-6361/202037607

- Skinner, S. L., Güdel, M., Briggs, K. R., & Lamzin, S. A. 2010, ApJ, 722, 1654, doi: 10.1088/0004-637X/722/2/1654
- Speagle, J. S. 2020, MNRAS, 493, 3132, doi: 10.1093/mnras/staa278
- Strom, K. M., & Strom, S. E. 1993, ApJL, 412, L63, doi: 10.1086/186941
- Szabó, Z. M., Kóspál, Á., Ábrahám, P., et al. 2021, ApJ, 917, 80, doi: 10.3847/1538-4357/ac04b3
- —. 2022, ApJ, 936, 64, doi: 10.3847/1538-4357/ac82f5
- Takasao, S., Hosokawa, T., Tomida, K., & Iwasaki, K. 2025, ApJ, 985, 16, doi: 10.3847/1538-4357/adc37b
- Travis, L. D., & Matsushima, S. 1968, ApJ, 154, 689, doi: 10.1086/149790
- Uchida, Y., & Shibata, K. 1984, PASJ, 36, 105
- Wachmann, A. 1954, ZA, 35, 74
- Welty, A. D., Strom, S. E., Edwards, S., Kenyon, S. J., & Hartmann, L. W. 1992, ApJ, 397, 260, doi: 10.1086/171785
- Whittet, D. C. B., Shenoy, S. S., Clayton, G. C., & Gordon, K. D. 2004, ApJ, 602, 291, doi: 10.1086/380837
- Xu, Z., Herczeg, G. J., Johns-Krull, C. M., & France, K. 2021, ApJ, 921, 181, doi: 10.3847/1538-4357/ac1739
- Yang, H., Herczeg, G. J., Linsky, J. L., et al. 2012, ApJ, 744, 121, doi: 10.1088/0004-637X/744/2/121
- Zhang, X., & Green, G. M. 2025, Science, 387, 1209, doi: 10.1126/science.ado9787
- Zhu, Z., Jiang, Y.-F., & Stone, J. M. 2020, MNRAS, 495, 3494, doi: 10.1093/mnras/staa952
- Zhu, Z., Stone, J. M., & Calvet, N. 2024, MNRAS, 528, 2883, doi: 10.1093/mnras/stad3712
- Zurlo, A., Weber, P., Pérez, S., et al. 2024, A&A, 686, A309, doi: 10.1051/0004-6361/202348526

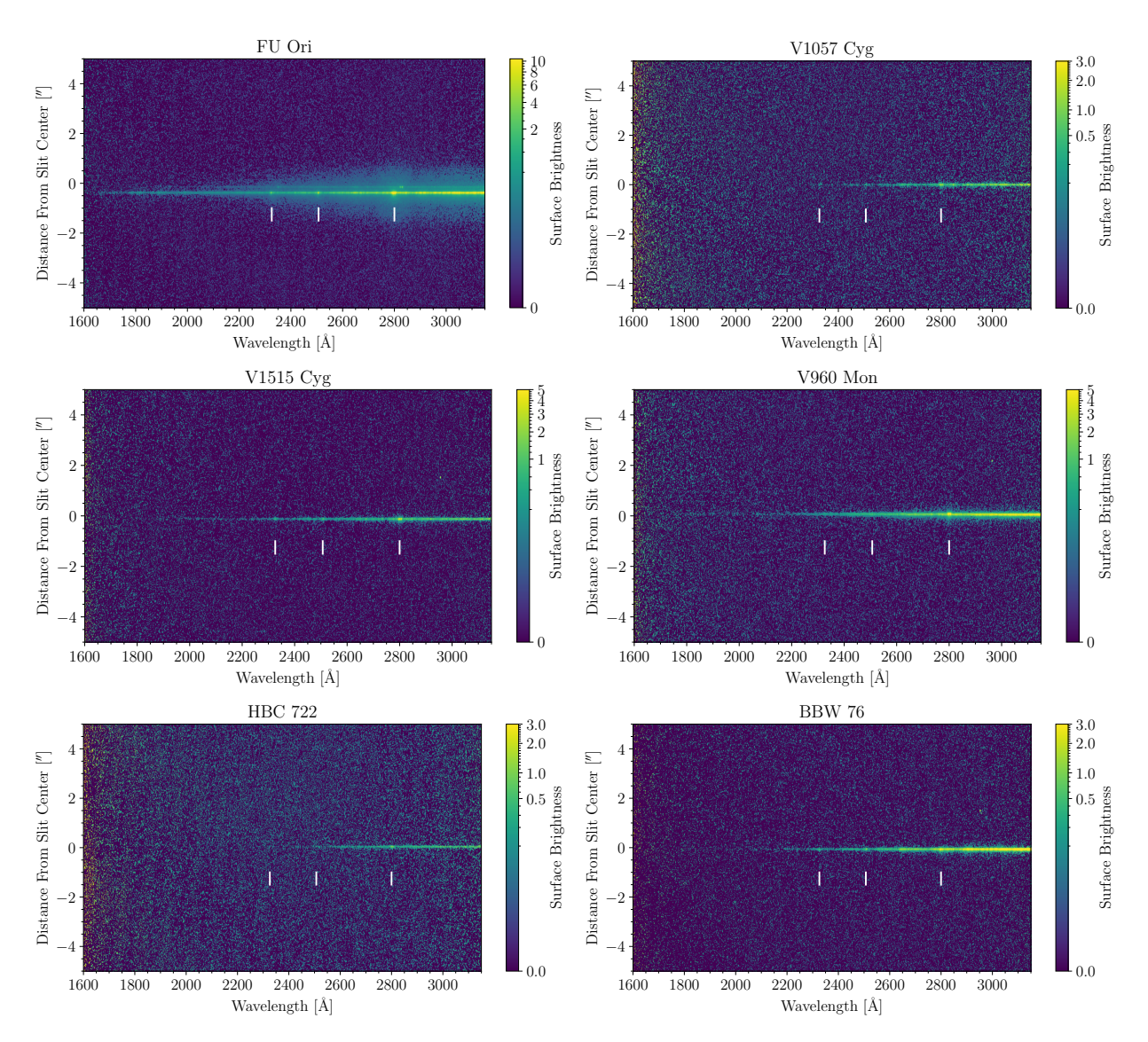


Figure A1. The two-dimensional rectified x2d HST/STIS images for each of our sources. The white hashes mark the locations of the C II] 2326, Fe II] 2500, and Mg II 2800 features and the surface brightness units are 10^{-14} erg s⁻¹ cm⁻² Å⁻¹ arcsec⁻². Notice that the traces of FU Ori, V1515 Cyg, and V960 Mon are all detected down to at 1800 Å. BBW 76 is only marginally detected at 2100 Å. V1057 Cyg is only detected redward of the C II feature, with barely any continuum until 2400 Å, and HBC 722 is only detected redward of 2450 Å.

APPENDIX

A. STIS 2D SPECTRA AND DETECTION CRITERIA FOR FAINTER SOURCES

The 2 dimensional recitified x2d G230L spectra of each object in the sample. For sources with 2 G230L exposures (see Table 1), the images have been coadded via an uncertainty-weighted mean. The traces can clearly be identified, as well as the 3 bright emission lines discussed in Section 4. In FU Ori, the diffuse emission from the bright scattered light nebula (Zurlo et al. 2024) can be seen, as well as the trace of FU Ori S (Carvalho et al. 2024a).

In order to check the wavelengths where the faintest 3 sources (V1057 Cyg, HBC 722, and BBW 76) were detected, we cut spatial profiles of the 2d spectra in \sim 78 Å bins. The spectrally-binned mean spatial profiles are shown in Figure A2. We then computed the maximum surface brightness (within 0.2'' of the slit center) and standard deviation (within 0.2'' of the slit center)

for each spatial profile. The source was considered "detected" in a given spectral bin if the maximum surface density was greater than $3\times$ the standard deviation.

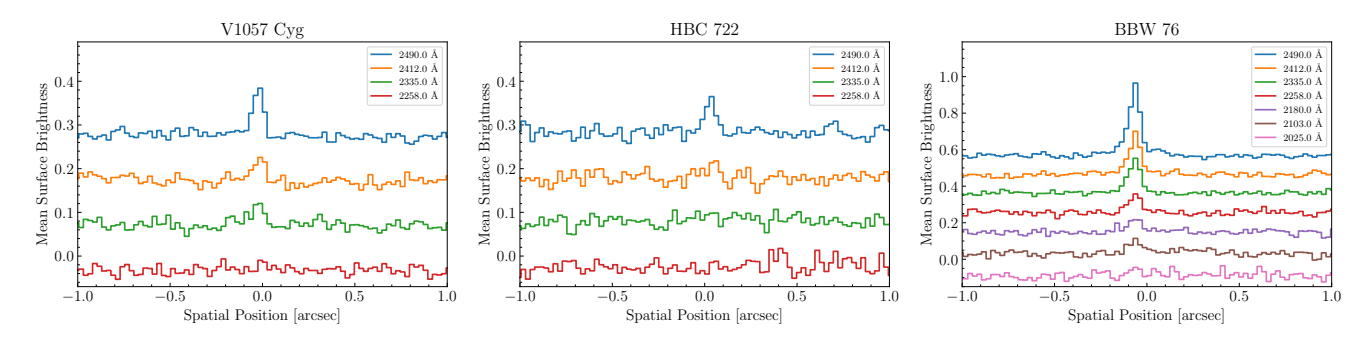


Figure A2. Spectrally averaged spatial cuts in the 2d spectra of V1057 Cyg (left), HBC 722 (middle) and BBW 76 (right). The spectral averaging was over ~ 75 Å and the legend shows the mean wavelength of each bin.

B. POSTERIOR DISTRIBUTIONS FOR THE UV EXCESS BLACKBODY FITS

The posterior distributions for the blackbody fits to the UV excess are shown in Figure B3 as corner plots (Foreman-Mackey 2016). Notice that for the sources with the strongest detected excess, the maximum temperature is poorly constrained by the NUV-only data. This is confirmed by the case of FU Ori, which has a well-constrained $T_{\rm BB}$ and $R_{\rm BB}$ in C24 when the fit included the FUV continuum but not in this paper when the fit is restricted to only the NUV. The luminosity of the emission, however, is clearly well-constrained. This can be seen from the fact that the posteriors of the $T_{\rm BB}$ and $T_{\rm BB}$ parameters lie along a locus well-described by $T_{\rm BB}$. The $T_{\rm BB}$ 0 posteriors reflect the priors, retrieving within errors the same values as the disk model best-fit values.

C. BP TAU AS A REPRESENTATIVE CTTS

We select BP Tau as our reference CTTS for the comparison between the NUV spectra of FUOrs and those of non-outbursting YSOs. The $M_* \sim 0.5~M_\odot$ of BP Tau is comparable to those of the central objects in our sample, while its accretion rate $(\dot{M}=10^{-7.29}~M_\odot~{\rm yr}^{-1})$ is typical for a CTTS (Manara et al. 2023).

To determine how well the NUV spectrum of BP Tau represents typical NUV spectra of CTTSs, we query all 87 of the STIS/G230L for sources classified as T Tauri Stars in the ULLYSES archive on MAST (Roman-Duval et al. 2025). The stellar properties of the sample span spectral types of M6 to A2 (though most are M2-K1) and a broad range of accretion rates.

We then perform a signal-to-noise selection, keeping only the 50 spectra that have a median signal-to-noise ratio of 5 for $\lambda > 2100$ Å. We divide each spectrum by an approximate continuum, estimated using the asymmetric least-squares fitting code described in (Carvalho et al. 2023a). We use an extremely inflexible regularization parameter of 10^12 and fit only the 10th percentile of flux, to avoid emission features and divide out only the general slope of each spectrum. We then interpolate each spectrum to a common wavelength grid and compute the 16th, 50th, and 84th percentile normalized flux over all spectra in each wavelength bin. This enables us to estimate the median spectrum in the sample as well as the typical object-to-object variation in features like strong emission lines.

Figure C4 shows the G230L spectrum of BP Tau compared with the median ULLYSES spectrum. The upper and lower ranges of spectra are shown in the shaded region. Notice that BP Tau almost perfectly matches the median spectrum.

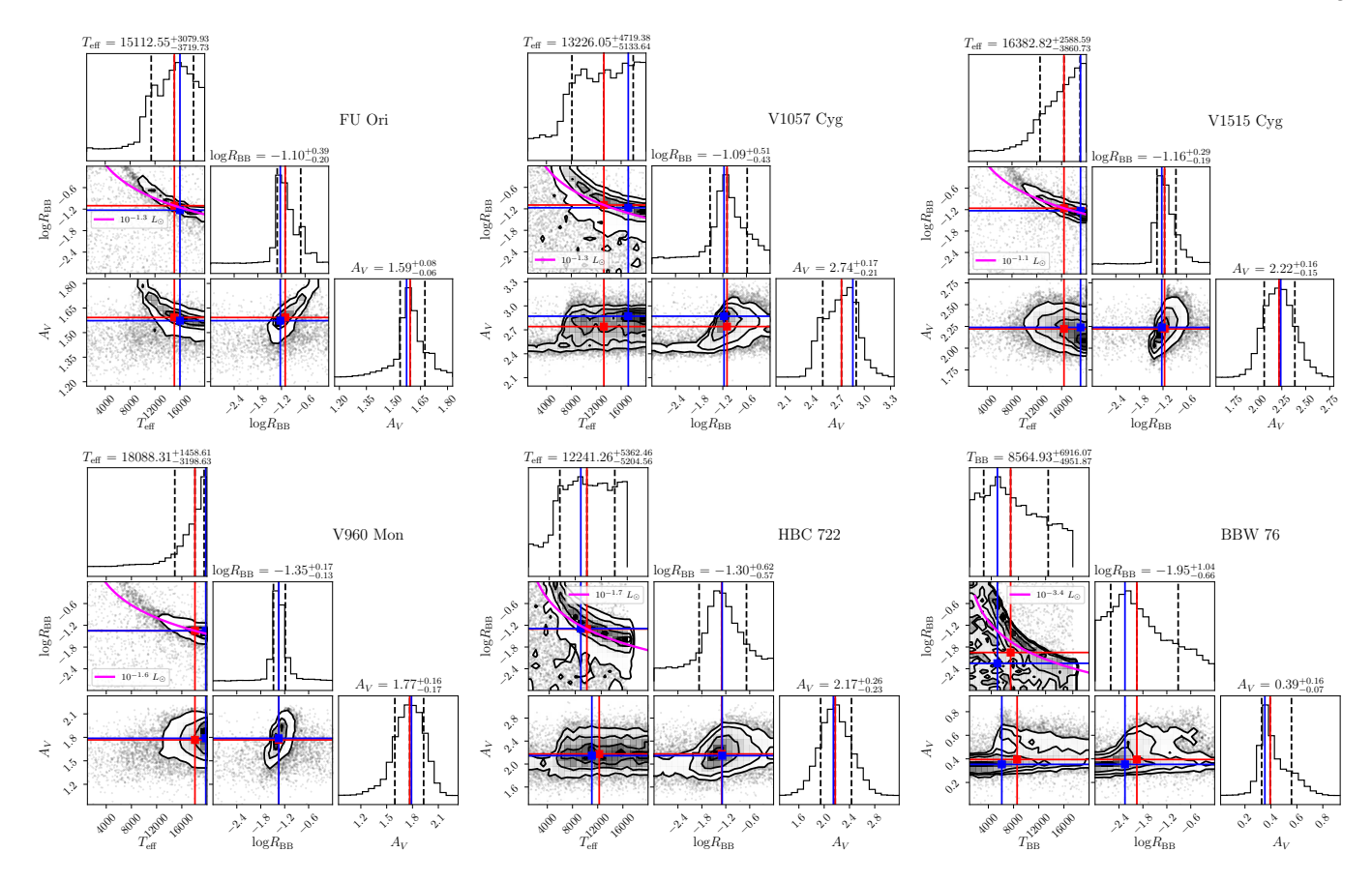


Figure B3. The posterior distributions for the blackbody fit described in Section 3.2. The red vertical and horizontal lines mark the median values for histogram, while the blue lines mark the modal values. The magenta line marks the $R_{\rm BB} \propto T_{\rm BB}^{-2}$ relation, anchored at the median $L_{\rm excess}$ value for each source.

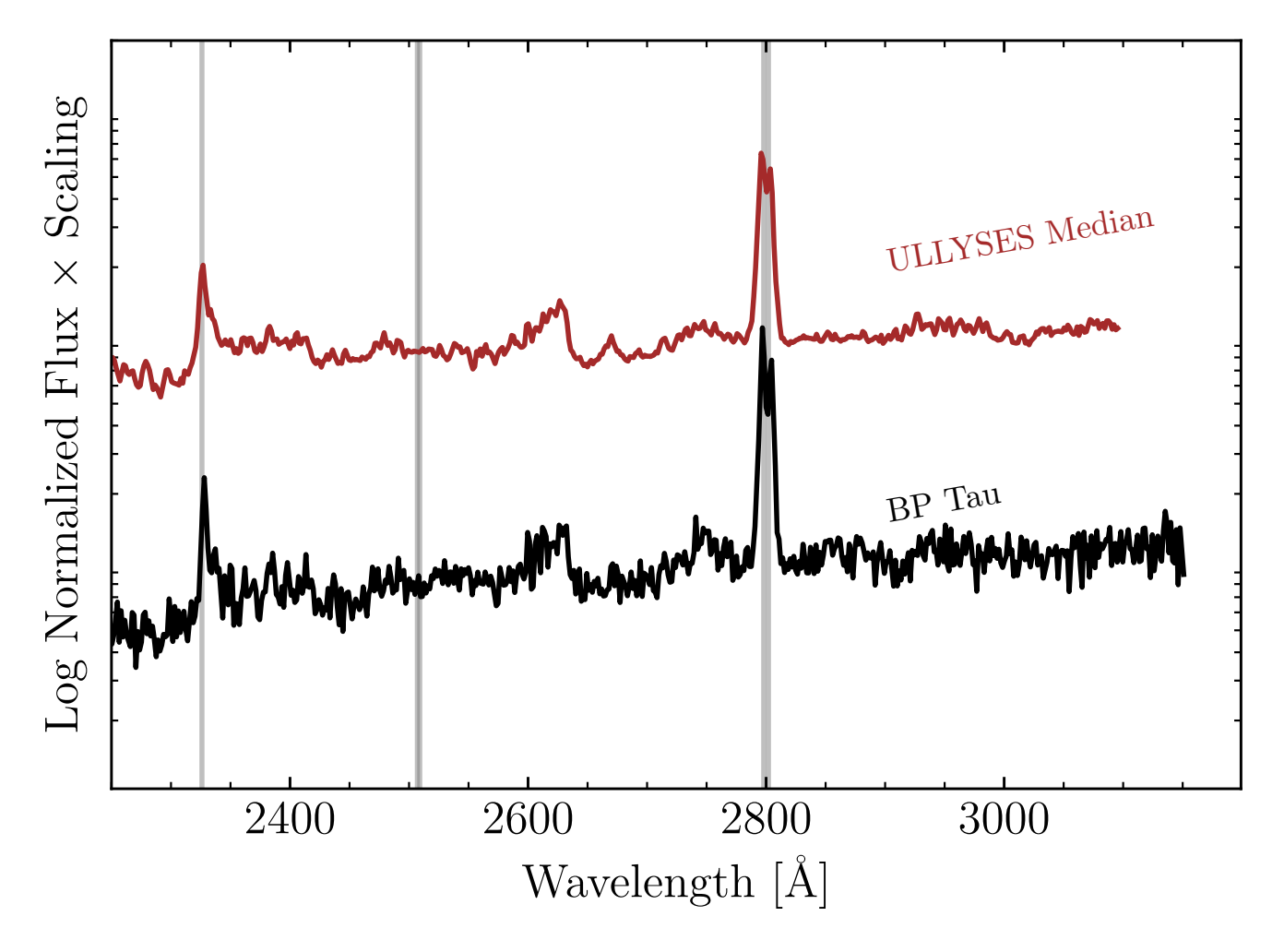


Figure C4. The G230L spectrum of BP Tau (black) compared with the median (brown line) and range (brown filled region) of G230L spectra of 50 CTTSs in the ULLYSES sample. The grey lines mark the locations of the NUV emission lines discussed in Section 4. Notice that there is no sign of the Fe II] emission feature at 2505 in either BP Tau or the ULLYSES sample.